Applied Magnetic Resonance (2020) 51:1515–1528
https://doi.org/10.1007/s00723-020-01266-2

Applied
Magnetic Resonance

ORIGINAL PAPER

Isolated Ti(III) Species on the Surface of a Pre-active Ziegler Natta Catalyst

Leonora Podvorica[1] · Enrico Salvadori[1] · Fabrizio Piemontesi[2] · Gianni Vitale[2] · Giampiero Morini[2] · Mario Chiesa[1]

Received: 27 June 2020 / Revised: 8 September 2020 / Accepted: 13 September 2020 /
Published online: 22 September 2020

Abstract

The nature of Ti(III) species, introduced in working models of industrial Ziegler Natta catalyst precursors, consisting of $MgCl_2/TiCl_4$ binary systems, eventually containing different Lewis basis, are studied by a combination of X- and Q-band CW and pulse EPR spectroscopy. In Ziegler Natta catalysts, Ti(III) play the double role of active catalytic species and unconventional spin probes. On the binary system, two dominant Ti(III) species, characterized by distinctively different EPR spectra, are observed. ^{35,37}Cl Q-Band HYSCORE spectra allow estimating the hyperfine and nuclear quadrupole interactions of directly coordinated Cl, characterized by a hyperfine dipolar contribution of the order of 5 MHz and nuclear quadrupole interactions of the order of $e^2qQ/h = 9$ MHz. Interestingly, the two dominant EPR active species are selectively suppressed by the presence of different Lewis bases, indicating the possibility to address the long standing issue of the influence of Lewis bases in driving specific morphological configurations and influencing the catalytic properties of Ti(III) active sites.

1 Introduction

"It is structure that we look for whenever we try to understand anything". This famous quote by Linus Pauling [1] underpins the issues which we are facing in understanding—more than 60 years after its discovery—the fine details of the Ziegler–Natta (ZN) olefin polymerization process.

Ziegler–Natta olefin polymerization is probably the most effective and atom-economical large-volume industrial chemical process and an almost unique example in chemistry of a development that arose from the synergy between fundamental

✉ Mario Chiesa
mario.chiesa@unito.it

[1] Department of Chemistry, University of Torino, Via Giuria 9, 10125 Torino, Italy

[2] Basell Poliolefine Italia S.R.L. LyondellBasell Group, G. Natta R&D Center, Piazzale G. Donegani 12, 44122 Ferrara, Italy

research and industrial efforts. However, despite the economic relevance of polyolefins, with a yearly market exceeding a billion dollar, a detailed understanding of the structure of the active sites in the heterogeneous catalyst is still missing.

This limited knowledge is a consequence of the complex structure of heterogeneous ZN catalysts and the elusive nature of the open-shell Ti(III) active species, formed during pre-catalyst activation. Efforts have been dedicated to characterize model systems [2–5], but this has only partially provided an insight into the complex, polycrystalline working catalysts at molecular level.

Modern industrial ZN catalysts are obtained by activating a pre-catalyst, consisting of $TiCl_4$ adsorbed on polycrystalline $MgCl_2$, with an Al-alkyl (AlR_3), typically $AlEt_3$ (Et = $-CH_2CH_3$). Lewis bases are added to the pre-catalyst to fine tune the catalytic activity and selectivity towards the amount and stereoregularity of the produced polypropylene.

Several questions are still open and can be summarized as follows: (i) which faces of $MgCl_2$ host the catalytically active Ti species; (ii) how these surfaces are modified by certain Lewis bases [often referred to as internal donors (ID)]; and (iii) by the AlR_3 co-catalyst. During this last stage, tetravalent Ti ions are reduced to a lower oxidation state [6] and both Ti(III) and Ti(II) have been proposed. Ti(III) centers are believed to play a pivotal role in ZN catalysis; however, their exact role and structure is still only vaguely defined. Their coordination environment and the interaction with Lewis bases and possibly, with fragments of the co-catalyst are all questions, which are still awaiting detailed answers. Due to the paramagnetic nature of Ti(III) ($3d^1$, $S = 1/2$), electron paramagnetic resonance (EPR) spectroscopy is in principle the ideal technique to answer such questions.

Conventional X-band continuous wave (CW) EPR techniques have been used primarily to monitor and quantify the amount of reduced Ti species [7–12]. However, modern EPR techniques offer a whole arsenal of specific experiments capable of investigating the local coordination environment of Ti(III) species in ZN catalysts [13–15].

The EPR identification of Ti(III) species that are formed in ZN catalysts—serving either as active sites or their precursors—is a non-trivial task as, upon activation with $AlEt_3$, different species are formed, most of which are EPR silent due to strong dipolar and exchange interactions. However, in the case of supported titanium–magnesium catalysts with a low titanium content (≤ 0.1 wt%), isolated mononuclear Ti(III) species have been reported to form on the surface at a high yield (40–70% of the total titanium content) [16]. Moreover, a correlation was found between the content of the isolated Ti(III) species and the activity of these catalysts in ethylene polymerization [16].

A characteristic feature of Ti(III) spectra is in that the g tensor is sensitive to both the coordination geometry and the nature of the ligands, reflecting the ligand field experienced by the paramagnetic ion. This sensitivity makes Ti(III) species in Ziegler Natta catalysts ideal probes to answer some specific questions related to the nature of the active species and their local environment. The observed g values for activated ZN catalysts depend on many factors, including the presence of coordinated AlR_3 co-catalysts, the potential coordination of Lewis basis, and the localization at different surface terminations of the $MgCl_2$ support. Tregubov et al. [11]

reported spectra with two Ti(III) signals with axial g tensor ($g_{\perp}^{1} = 1.984$, $g_{\perp}^{2} = 1.966$ and $g_{\parallel}^{1,2} = 1.79$) for a supported $TiCl_4/MgCl_2$ system obtained by the reduction with triisobutylaluminium (TIBA), while a rhombic spectrum with $g_1 = 1.830$, $g_2 = 1.889$, and $g_3 = 1.978$ was reported for $TiCl_3$ dissolved in absolute methanol [17]. EPR spectra of the $TiCl_3 \cdot 0.3AlCl_3$ catalyst showed a signal with $g_{\perp} = 1.94$ and $g_{\parallel} = 1.90$ (with a concentration of just 1% of the total titanium content) [18]. Dilution with $MgCl_2$ resulted in the dispersion of titanium trichloride and increased spectral resolution resulting in a slightly rhombic spectrum with $g_1 = 1.94$, $g_2 = 1.92$, and $g_3 = 1.90$.

In the case of the reductive activation of Ti containing pre-catalysts, complex EPR spectra are commonly observed, characterized by a set of signals with a wide range of g values, from 1.89 to 1.99. These signals stem from different families of Ti(III) species formed during the reductive activation of the sample, comprising Ti(III) at different surface terminations and with different local environments.

As part of a general study of the properties of open-shell species in ZN catalytic systems and to address the aforementioned issues, we explore the nature of Ti(III) species introduced in $MgCl_2/TiCl_4$ catalyst precursors, eventually containing different Lewis bases by a combination of X- and Q-band CW and pulse EPR spectroscopy. The main scope of the work is to provide insight in the local coordination of Ti(III) in relevant catalyst systems, correlating the EPR features, including $^{35,37}Cl$ hyperfine interactions obtained via HYSCORE experiments with the nature of the sample.

2 Experimental

2.1 Samples

The $MgCl_2/TiCl_4$/ID (ID = aliphatic monoether or aliphatic diester) samples and the ID free counterpart containing Ti(III) species were prepared in the laboratories of Giulio Natta R&D Centre of Basell Poliolefine Italia following standard procedures. They represent working models similar to industrial solid catalyst precursors.

2.2 EPR Measurements

X-Band CW-EPR spectra were detected at room temperature with a Bruker ESP 300E spectrometer operating at a microwave frequency 9.5 GHz. The X-band CW-EPR measurements were performed at RT with a microwave (mw) power of 10.1 mW, a modulation frequency of 100 kHz, and a modulation amplitude of 0.1 mT.

The Q-band measurements were performed on a Bruker Elexys E580 spectrometer operating at a microwave frequency of 34 GHz. The EPR spectrometer is equipped with helium gas-flow cryostats (Oxford, Inc.).

Electron-spin-echo (ESE)-detected EPR experiments were carried out with the pulse sequence: $t_{\pi/2} - \tau - t_{\pi} - \tau -$ echo. For the Q-band experiments, the mw pulse

lengths $t_{\pi/2} = 16$ ns and $t_{\pi} = 32$ ns and a τ value of 200 ns were used. The shot repetition rate adopted for the experiments was 1 kHz and $T = 50$ K.

Three-pulse ESEEM measurements were carried out at Q-band by increasing the time delay T of the pulse sequence: $t_{\pi/2} - \tau - t_{\pi/2} - T - t_{\pi/2} -$ echo, with $t_{\pi/2} = 16$ ns. The time interval T was varied in steps of 8 ns starting from 100 ns. A four-step phase cycle was used to eliminate unwanted echoes. To avoid blind spot effects, two-dimensional three-pulse ESEEM spectra were recorded as a function of the interpulse delay τ, which was varied from 100 to 212 ns in steps of 8 ns. Two dimensional ESEEM spectra were obtained by sweeping the magnetic field from 1200 to 1320 mT (70 data points). In this case, a fixed interpulse delay $\tau = 188$ ns was chosen based on the three-pulse vs τ experiment. A 1 kHz repetition rate was used for all experiments. Further experimental details are specified in the figure captions.

HYSCORE experiments [19] were carried out at Q-band with the pulse sequence $t_{\pi/2} - \tau - t_{\pi/2} - t_1 - t_{\pi} - t_2 - t_{\pi/2} - \tau -$ echo with the microwave pulse lengths $t_{\pi/2} = 16$ ns and $t_{\pi} = 32$ ns. The time intervals t_1 and t_2 were varied in steps of 16 ns starting from 96 to 4896 ns with a repetition rate of 1 kHz. An interpulse delay $\tau = 188$ ns was used based on the three-pulse vs. τ experiment. A four-step phase cycle was used to eliminate unwanted echoes. The time traces of the HYSCORE spectra were baseline corrected with a third-order polynomial, apodized with a Hamming window and zero filled. After two-dimensional Fourier transformation, the absolute value spectra were calculated. All EPR and HYSCORE spectra were simulated using the Easyspin simulation package [20].

3 Results and Discussion

Studying Ti(III) species in supported titanium sites on $MgCl_2$ provides insight into the typical EPR parameters that can be used for interpreting the results of the more complex activated catalysts. In this study, we, therefore, exploit the presence of Ti(III) species introduced during the impregnation of the $MgCl_2$ support with $TiCl_4$ to explore the relation between the EPR spectral features and the nature of the sample. In particular, three systems are considered: a binary system $MgCl_2/TiCl_4$ and two ternary systems where two different Lewis bases—a diester or a monoether—were incorporated.

Grafting of $TiCl_4$, in principle, can occur at different surface terminations of $MgCl_2$ and the actual facets hosting the catalytically active Ti species remain to a large extent matter of controversy. The (104) and (110) facets have been identified as the relevant surfaces, with some authors proposing that specific point defects localized on such surfaces are the relevant adsorption sites [21, 22]. The (015) surface has also been proposed as an alternative relevant surface [23].

In general, consensus has been reached about (104) surfaces, exposing penta-coordinated magnesium sites, as being thermodynamically more stable than (110) surfaces, exposing tetra-coordinated magnesium sites [23, 24]. However, this energetic scenario is known to be profoundly altered by the adsorption of Lewis bases, favoring the (110) sites. Computational and experimental results show a preferential binding of $TiCl_4$ monomers to the (110) surface [25], resulting in a

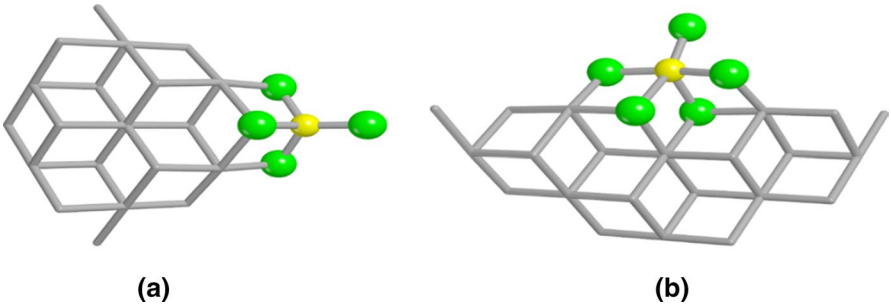

Fig. 1 Schematic representation of possible coordination modes of Ti(III) at a) (104) $MgCl_2$ surface and b) on a (110) surface. Color code: Cl, green; Ti, yellow

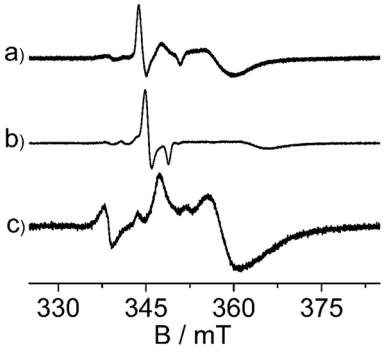

Fig. 2 Normalized X-band CW-EPR spectra of Ti(III) in **a** $MgCl_2/TiCl_4$ binary system, **b** $MgCl_2/TiCl_4$/monoether ternary system, and **c** $MgCl_2/TiCl_4$/diester ternary system

pseudo-octahedral titanium site or, in the case of a complexed $TiCl_3$ monomer, in a distorted pyramidal coordination. On the other hand, coordination at the (104) $MgCl_2$ termination would give a tetrahedral coordination of the Ti(III) ions [14]. The two different titanium coordination modes are shown in Fig. 1.

The X-band CW-EPR spectra of Ti(III) recorded for the different systems are shown in Fig. 2.

All spectra show the presence of a weak isotropic signal resonating at $g = 2.003$ (337.5 mT) which is assigned to radical impurities. The intensity of the radical species was found to vary in the different samples being particularly intense in the ternary system containing the diester Lewis bases (Fig. 2c).

The spectrum of Ti(III) in the binary $MgCl_2/TiCl_4$ mixture is reported in Fig. 2a and features a complex EPR powder pattern indicating the presence of at least two EPR active species. These are characterized by g values and line widths typical of isolated Ti(III) species but experiencing different local environments. A dramatic change in the spectrum is observed for Ti(III) at the ternary system $MgCl_2/TiCl_4$/monoether (Fig. 2b). In this case, the spectrum is dominated by a single species with axial symmetry and $g_\perp > g_\parallel$. The reversed situation is observed for the ternary system $MgCl_2/TiCl_4$/diester (Fig. 2c). In this case, the spectrum is dominated by the spectral pattern of the second species, which displays a pseudo-axial symmetry with $g_\perp < g_\parallel$. This comparison reveals that in the binary system, two Ti(III) species with

different EPR symmetry are present, while the introduction of the Lewis bases selectively suppresses one of the two species, depending on the nature of the molecule.

To obtain the spin-Hamiltonian parameters of the different species, computer simulation of the CW-EPR spectra at X-band and of the corresponding Q-band ESE spectra were carried out.

3.1 *The $MgCl_2$/$TiCl_4$ Binary System*

The experimental and simulated spectra are shown in Fig. 3, while the spin-Hamiltonian parameters extracted from the simulation are listed in Table 1. The spectra are characterized by the presence of two overlapping signals due to two different Ti(III) species and a sharp resonance at $g = 2.003(4)$ assigned to a radical species. The two Ti species contributing the EPR spectrum are labeled Ti(III)-***A*** and Ti(III)-***B*** and are indicated by stick diagrams in Fig. 3, while the radical species is indicated with *R*. The simulations of the spectra recorded at the two different frequencies were carried out using the same set of spin-Hamiltonian parameters, only changing the line-width and the relative abundance of the species. This is justified, because both depend on the frequency-dependent relaxation properties and different experimental conditions. The relative abundance of the different species reported in Table 1 is referred to the simulation of the X-band CW spectra.

In the case of Ti(III), due to the low natural abundance of the magnetically active isotopes (^{47}Ti $I = 5/2$, natural abundance 7.75%, and ^{49}Ti $I = 7/2$, natural abundance 5.51%), the information derived from the CW-EPR powder spectrum is usually limited to the electron Zeeman interaction, which is a useful reporter of the symmetry of the site.

In the classical crystal-field theory, the EPR parameters are explained using the perturbation formulas based on the one-spin–orbit (SO)-parameter model [26]. Under the effect of a tetrahedral crystal field, the five *d* orbitals are split to give a set of two degenerate orbitals (d_{z2}, d_{x2-y2}) and a set of three degenerate orbitals (d_{xy}, d_{xz}, d_{yz}). The effect of a further tetragonal distortion stabilized the d_{z^2} orbital in case of

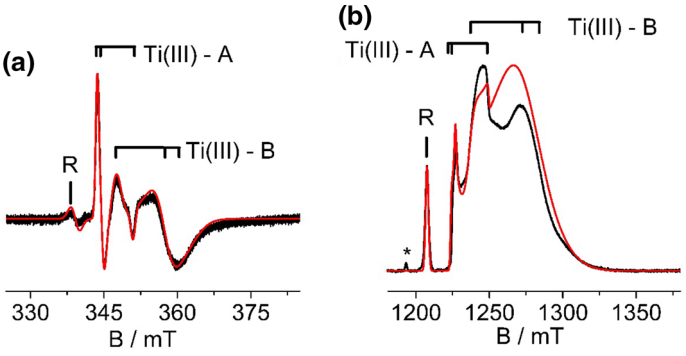

Fig. 3 Experimental (black) and computer simulated (red) EPR spectra of Ti(III) species in the $MgCl_2$/$TiCl_4$ binary system. **a** X-band CW-EPR; **b** Q-band ESE detected EPR. The stick diagrams indicate the two dominant Ti species, R the radical, and * a spurious signal of the Q-band cavity

Table 1 Spin-Hamiltonian parameters obtained from the simulation of the EPR spectra of Ti(III) in the three samples

Sample	Species	g_x	g_y	g_z	%ab
$MgCl_2/TiCl_4$	Ti(III)				
	A	1.977 (3)	1.971 (8)	1.936 (0)	14.1
	B	1.88 (0)	1.89 (9)	1.954 (4)	84.7
	R	2.003 (4)	2.003 (4)	2.003 (4)	1.2
$MgCl_2/TiCl_4$ aliphatic monoether	Ti(III)				
	A	1.977 (3)	1.977 (3)	1.936 (0)	11.0
	A′	1.969 (3)	1.966 (0)	1.946 (3)	55.4
	C	1.8 (7)	1.8 (7)	1.8 (7)	33.0
	R	2.003 (7)	2.003 (7)	2.003 (7)	0.6
$MgCl_2/TiCl_4$ aliphatic diester	Ti(III)				
	A	1.977 (3)	1.977 (3)	1.936 (0)	0.4
	B	1.88 (0)	1.89 (9)	1.954 (4)	94.2
	D	1.954 (5)	1.925 (8)	1.849 (0)	3.0
	R	2.003 (4)	2.003 (4)	2.003 (4)	2.4

The relative abundance of the different species refers to the CW X-band EPR experiments

a compression, or the $d_{x^2-y^2}$ orbital in case of an elongation. Considering the distortion axis along the *z*-direction, the *g* values are given, to first order, by the following equations in the case of tetragonal compression and elongation, respectively:

$$g_{\parallel} \cong g_{\mathrm{e}} \text{ and } g_{\perp} \cong g_{\mathrm{e}} - \frac{6\lambda}{\Delta_{\mathrm{Td}}} \tag{1}$$

$$g_{\parallel} \cong g_{\mathrm{e}} - \frac{8\lambda}{\Delta_{\mathrm{Td}}} \text{ and } g_{\perp} \cong g_{\mathrm{e}} - \frac{2\lambda}{\Delta_{\mathrm{Td}}}. \tag{2}$$

In Eqs. 1 and 2, λ is the spin–orbit coupling constant (154 cm^{-1} for Ti^{3+}), $g_e = 2.0023$ is the free electron *g* value, and Δ_{Td} is the energy separation between the degenerate triplet and doublet levels in the cubic tetrahedral field. Thus, for a tetrahedral coordination geometry with tetragonal compression $g_{\perp} < g_{\parallel} \cong g_e$ is expected (Eq. 1), while for a tetragonal elongation $g_{\parallel} < g_{\perp} < g_e$ (Eq. 2). In our case, we observe a significant departure from g_e suggesting that a d_{z^2} ground state is unlikely.

On the other hand, in the case of an octahedral coordination and tetragonal compression, the ground state is the d_{xy} orbital, while if the distortion is a tetragonal elongation, the ground state is a degenerate d_{xy}, d_{yz} orbital, subjected to Jahn–Teller effect that further resolves the degeneracy [27–30]. The *g* value expressions for a Ti^{3+} ion in a tetragonally distorted octahedral environment are thus:

$$g_{\parallel} \cong g_e - \frac{8\lambda}{\Delta} \text{ and } g_{\perp} \cong g_{\mathrm{e}} - \frac{2\lambda}{\delta} \tag{3}$$

where Δ and δ are the energy separation between the t_{2g} (octahedral field) and e_g (tetragonal distortion) d orbitals. Although the actual situation may be more complicated than what described in Eqs. 1–3 due to lower local symmetry, these may provide some useful guidelines to determine the ground state of the Ti(III) species. In particular, based on this analysis, Ti(III)-***A*** ($g_\perp > g_\parallel$) is amenable to a d_{x2-y2} or d_{xy} ground state associated with tetrahedral or octahedral coordination respectively, while Ti(III)-***B*** ($g_\perp < g_\parallel$) can be associated with a d_{xy} ground state associated with a octahedral coordination, provided that $\Delta > 4\delta$. In other words, Ti(III)-***B*** can only be associated with a pseudo-octahedral coordination, while Ti(III)-*A* may be related to both octahedral or tetrahedral coordination.

To investigate in more detail the nature of the Ti(III) species, ESEEM and HYSCORE experiments were performed. A first hint about the magnetic nuclei surrounding the Ti(III) is obtained from Q-band field-dependent three-pulse ESEEM (Fig. 4).

The spectrum shows a rich ESEEM pattern with features in the range from 0 to about 10–15 MHz, across the entire spectrum, indicating the presence of hyperfine interactions. The only magnetically active nuclei in the sample are ^{1}H and ^{35,37}Cl, all other nuclei having too low a natural abundance. Given that the ^{1}H Larmor frequency at the operational field is in the range 51–54 MHz, the complex spectral pattern is due to the interaction of the unpaired electron with ^{35,37}Cl nuclei ($I = 3/2$). The three pulse versus two pulse spectrum taken at a field position corresponding to the narrowest feature of the ESE spectrum ($B_0 = 1227.4$ mT) is shown in Fig. 4b. The sum projected three-pulse ESEEM spectrum (bottom of Fig. 4b) presents three peaks with different amplitudes and widths. The narrow peak at $\nu = 4.2$ MHz corresponds to the Larmor frequency of ^{37}Cl and is due to coupling with remote (matrix) Cl nuclei. The remaining peaks at 7.1 MHz and 13.3 MHz must arise from the interaction of directly coordinated chlorines. To further elucidate the nature of these transitions, HYSCORE experiments were performed at this field and at another field position ($B_0 = 1246.0$ mT).

The HYSCORE spectra recorded at two different magnetic field settings are shown in Fig. 5. The magnetic fields at which the two HYSCORE experiments were

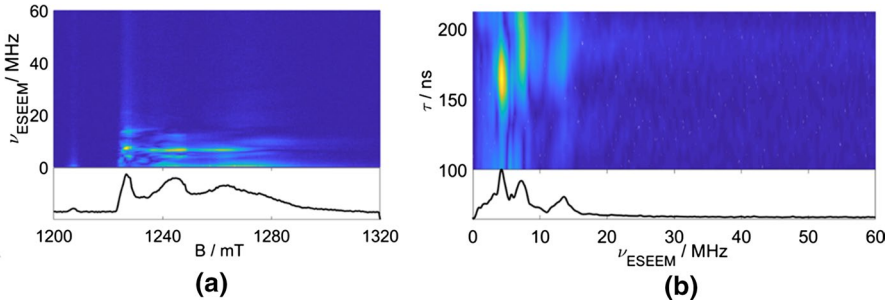

Fig. 4 **a** Three-pulse ESEEM spectrum plotted in the frequency domain versus the resonant magnetic field, **b** three pulse vs. the interpulse delay τ taken at $B_0 = 1227.4$ mT. The spectra were recorded at 10 K and Q-band frequency ($\nu = 33.8$ GHz)

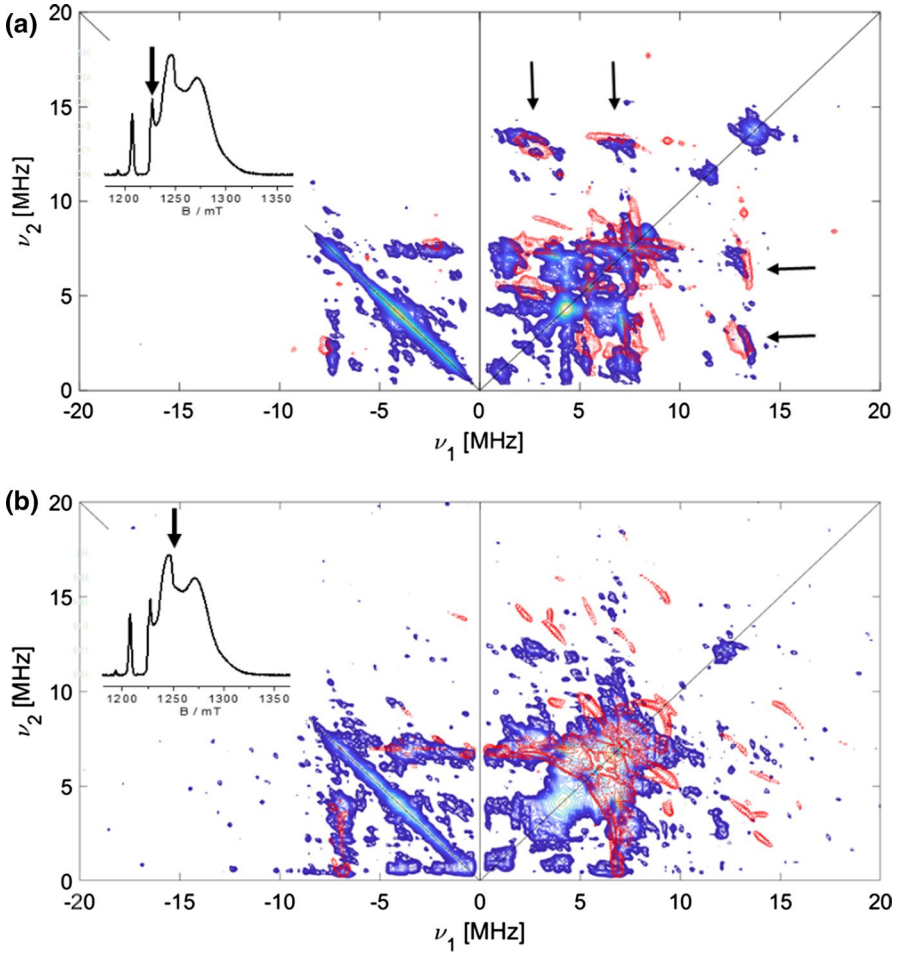

Fig. 5 Q-band HYSCORE spectrum recorded at **a** 1227.4 mT and **b** 1246.0 mT. Spectra were recorded at 10 K and an interpulse delay $\tau = 188$ ns. The simulations were obtained with the following parameters $A = [-5\ -5\ 8.5]$MHz, α, β, γ [0 10 0], $e^2qQ/h = 8.8$ MHz, $\eta = 0$, α, β, γ [0 20 0], where α, β, and γ are the Euler angles in degree, relating the orientation of the A and Q tensor axes with respect to the g tensor frame. Simulations account for both ^{35}Cl and ^{37}Cl isotopes in their natural abundance. The reported hyperfine values refer to the most abundant ^{35}Cl isotope. The arrows in **a** indicate single–double quantum transitions. In the insets the two positions at which the HYSCORE spectra were recorded is indicated

performed are shown in the insets of Fig. 5. Based on the three pulse vs τ experiment, the spectra were recorded with an interpulse delay $\tau = 188$ ns which limits the suppression effects of the relevant ESEEM frequencies. The spectrum recorded at a field position coinciding with that of the ESEEM spectrum of Fig. 4b [$B_0 = 1227.4$ mT, corresponding to the g_x, g_y components of species Ti(III)-A], shows a complex set of cross peaks in the (+,+) quadrant, arising from the interaction of ^{37,35}Cl nuclei. A series of peaks appearing at frequencies (1.9, 13.3) MHz, (13.3, 1.9) MHz, and (7.1, 13.3) MHz, and (13.3, 7.1) MHz in the bidimensional spectrum of Fig. 5a

(indicated by arrows) is assigned to single–double quantum transitions. The narrow peaks and high resolution of the spectra point to well-defined species, reminiscent of molecular systems found in solution. The HYSCORE spectrum in Fig. 5b was recorded at $B_0 = 1246.0$ mT, corresponding to the g_z component of species Ti(III)-A, partially overlapped with that of Ti(III)-B, leading to the particularly complex situation where contributions from both species are simultaneously present. Despite the high resolution of the experimental spectra, the extraction of reliable spin-Hamiltonian parameters is not an easy task in light of the significant anisotropic hyperfine interaction expected for Ti-Cl species, fairly large nuclear quadrupole couplings [14, 18], and the presence of overlapping species. Our approach to the analysis, therefore, was to simulate the HYSCORE spectra, taking reliable data previously obtained by some of us in the case of $TiCl_3$ molecular complexes and validated by DFT calculations [14, 18] as an initial approximation and trying to reach an agreement between the simulated and experimental spectra. The nuclear quadrupole interaction parameters were varied in broad limits to obtain an understanding of the strength of this interaction. Obviously, given all the above considerations, we did not aspire to really fit the experimental HYSCORE spectra, but rather, to achieve a qualitative resemblance between the simulations and experiments. We find that the experimental spectra taken at the two observer positions can be reasonably simulated with a single set of hyperfine and quadrupole values, corresponding to values determined for $TiCl_3$ molecular species and Ti(III) in ZN catalysts previously studied by some of us [14, 18]. An example of a reasonable simulation is shown in red in Fig. 5, superimposed to the experimental spectra. The simulation was obtained introducing a Cl hyperfine-interaction tensor characterized by a fairly large dipolar component, relatively small Fermi contact contribution ($A = [-5\ -5\ +8.5]$ MHz) and nuclear quadrupole interaction values (e^2qQ/h) in the range 7–12 MHz. These values are lower than those recently reported in a detailed NMR study for $TiCl_3$ ($e^2qQ/h = 14.5$ MHz) [31] but consistent with values obtained for an activated ZN catalyst [14].

In summary, the following conclusions can be drawn for the hyperfine and nuclear quadrupole interactions of Ti(III)-Cl species in the $MgCl_2/TiCl_4$ binary system. The anisotropic hyperfine tensor is similar to that estimated and computed for molecular $TiCl_3$ species in solution [18], with a dipolar component T of the order of 5 MHz and small a_{iso} of less than 1 MHz The nuclear quadrupole interaction tensor is close to axial and the coupling constant e^2Qq/h is of the order of 9 ± 2 MHz with its main axis nearly parallel to the main axis of the anisotropic hyperfine tensor.

3.2 *$MgCl_2/TiCl_4$/Monoether Ternary System*

In the case of ternary systems, $MgCl_2/TiCl_4$/Aliphatic monoether, the presence of the Lewis base, induces a significant change in the EPR spectrum. The simulation of the CW X-Band and Q-Band ESE spectra are shown in Fig. 6 and indicate a substantial suppression of the Ti(III)-***B*** species and appearance of a new and relatively broad signal centered at $g = 1.87$ and indicated as Ti(III)-C in Fig. 6. Given the broad line-width of this signal no significant details can be extracted from the simulation and this species will not be discussed further.

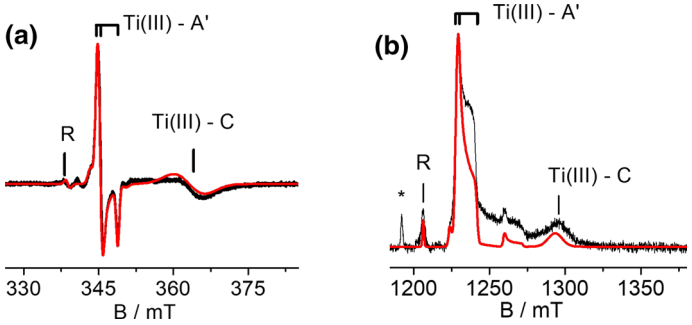

Fig. 6 Experimental (black) and computer simulated (red) EPR spectra of Ti(III) species in the $MgCl_2$/$TiCl_4$/monoether ternary system :**a** X-band CW-EPR spectra; **b** Q-band ESE detected EPR spectra. The stick diagrams indicate the dominant Ti species, *R* the radical, and * a spurious signal of the Q-band cavity

Moreover, the spin-Hamiltonian parameters (listed in Table 1) of species Ti(III)-***A*** are perturbed indicating a slight modification in the local coordination environment. The *g* tensor component of this species, indicated as Ti(III)-**A′**, are shown in Fig. 6 by a stick diagram.

The HYSCORE spectrum recorded at the maximum echo intensity (corresponding to the $g_\perp$ component of the EPR spectrum of species Ti(III)-**A′**) is shown in Fig. 7. At variance with the case of the binary system, the spectrum is characterized by a pair of relatively weak cross peaks at (3, 7.1) MHz and (7.1, 3) MHz, which correspond to single quantum transitions observed in the spectrum of the binary system. The overall intensity of the HYSCORE spectrum is lower than the

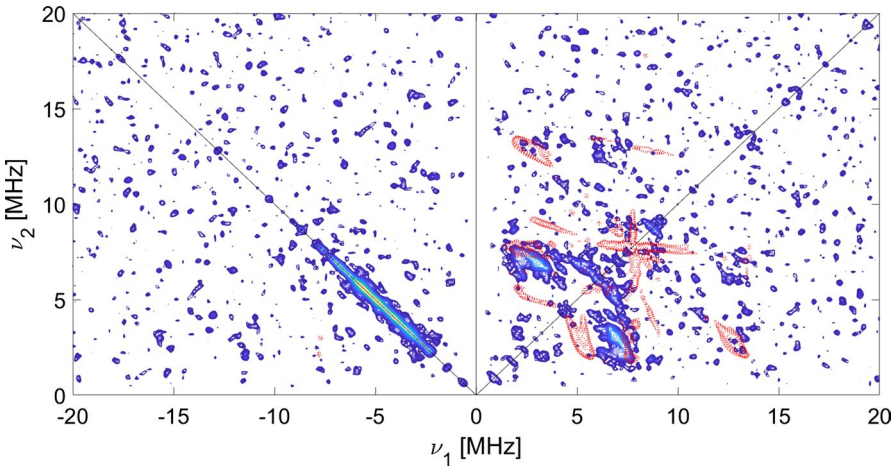

Fig. 7 Q-band HYSCORE spectrum of the ternary system $MgCl_2$/$TiCl_4$/monoether recorded at 1227.4 mT at 10 K and with an interpulse delay $\tau = 200$ ns. Due to the low signal intensity, the spectrum was symmetrized to better identify the correlation peaks. The simulation was obtained using the same parameters reported in Fig. 5, with the intensity adjusted to match that of the experimental spectrum

one observed for the binary system and the presence of single–double quantum correlation peaks barely observable. The lower intensity of the Cl cross peaks may be ascribed to a reduced number of coordinated chlorine, which may be an indication of the presence of the Lewis base in the first coordination sphere of Ti(III). This would concur with the slight *g*-shift observed in the EPR spectrum. However, as HYSCORE experiments do not provide specific evidence for the direct coordination of the monoether to Ti(III) further experiments, possibly involving isotopic substitution, will be needed to clarify this point.

3.3 *$MgCl_2$/$TiCl_4$/Diester Ternary System*

Finally, in the case of the ternary system $MgCl_2$/$TiCl_4$/diester, the EPR spectra presented in Fig. 8 evidence the selective suppression of the Ti(III)-***A*** species. The spectrum is dominated by the broad resonances of the quasi-axial species Ti(III)-**B**, which accounts for the 94% of the total spectral intensity. The simulation of the spectrum also indicates the presence of additional species, with abundance of the order of 3% (species Ti(III)-**D**). The spin-Hamiltonian parameters obtained from the simulation and the relative abundance of the species are collected in Table 1.

The Q-band echo spectrum (Fig. 8b) has a relatively low intensity, so that the HYSCORE spectra in this case were non-informative.

4 Conclusions

We studied the nature of open-shell Ti(III) species on a series of ZN pre-catalysts before activation. Ti(III) species were employed as unconventional self-reporting spin probes to detect the influence of different Lewis bases on the nature of the Ti(III) species. On the binary system $MgCl_2$/$TiCl_4$, we observe two dominant Ti(III) species, characterized by distinctively different EPR spectra. Species Ti(III)-***A*** characterized by a pseudo-axial EPR spectrum with $g_\perp > g_\parallel$, and species Ti(III)-***B***

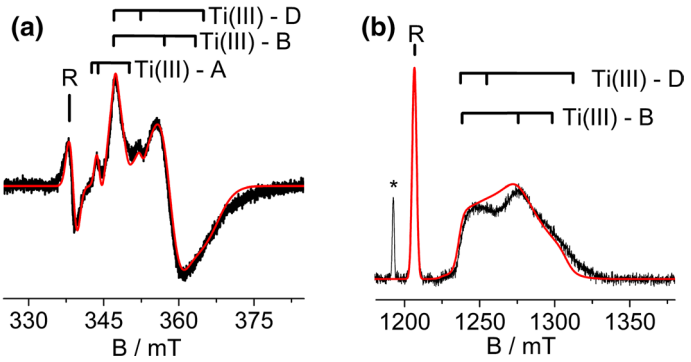

Fig. 8 Experimental (black) and computer simulated (red) EPR spectra of Ti(III) species in the $MgCl_2$/$TiCl_4$/diester ternary system. **a** X-band CW-EPR spectra; **b** Q-band ESE detected EPR spectra. The stick diagrams indicate the different Ti species, *R* the radical, and * a spurious signal of the Q-band cavity

characterized by a reversed g symmetry with $g_{\perp} < g_{\parallel}$. Both species are characterized by a Cl rich environment revealed by ^{35,37}Cl Q-Band HYSCORE spectra. The complex spectra were simulated taking literature values as initial guesses and can be understood in terms of a hyperfine coupling tensor with a dominant hyperfine dipolar contribution of the order of 5 MHz and nuclear quadrupole interactions of the order of $e^2qQ/h = 9$ MHz. Analysis of the g tensor indicates that Ti(III)-***B*** can only be associated with a pseudo-octahedral coordination, while Ti(III)-***A*** may be related to both octahedral or tetrahedral coordination. These differences point thus to the localization of the Ti(III) species at different terminations of the $MgCl_2$ substrate. Indeed, it would be tempting to associate the two species with the well-known stable terminations of $MgCl_2$, i.e., the (110) and (104) facets. This assignment cannot, however, be safely done at this stage, given the limited amount of information relative to the local morphology of the catalyst precursor. Remarkably, these two species are selectively suppressed by the presence of different Lewis bases. When a monoether is present, species Ti(III)-***B*** is suppressed, while the opposite happens in the presence of a diester. This observation is important as directly reveals a preferential adsorption of different Lewis bases in ZN catalysts, which, in turn, directly influences the nature of Ti(III) species. This not only highlights the role of Ti(III) species as local structural spin probes of complex ZN catalysts, but represents a starting point for clarifying the influence of specific Lewis bases in determining the nature of Ti(III) active sites. A systematic study of the influence of different Lewis bases on the EPR properties of Ti(III) surface species will be thus the subject of future investigations aimed at clarifying the long standing question of the surface localization of catalytically active species in ZN catalysts and the influence of Lewis bases in driving specific morphological configurations.

Acknowledgements This work is part of a project that has received funding from the European Union's Horizon 2020 research and innovation programme under the Marie Skłodowska-Curie Grant agreement no. 813209

Funding Open access funding provided by Università degli Studi di Torino within the CRUI-CARE Agreement.

References

1. L. Pauling, Main Curr. Mod Thought **7**, 108 (1950)
2. T. Risse, J. Schmidt, H. Hamann, H.J. Freund, Angew. Chem. Int. Ed. **41**, 1517 (2002)
3. E. Magni, G.A. Somorjai, J. Phys. Chem. **100**, 14786 (1996)

4. E. Magni, G.A. Somorjai, Catal. Lett. **35**, 205 (1995)
5. S.H. Kim, G.A. Somorjai, Surf. Interface Anal. **31**, 701 (2001)
6. C. Beermann, H. Bestian, Angew. Chemie **71**, 618 (1959)
7. P. Brant, A.N. Speca, Macromol. **20**, 2740 (1987)
8. J.C.W. Chien, J.C. Wu, C.I. Kuo, J. Polym. Sci. Part A Polym. Chem. **20**, 2019 (1982)
9. P. Šindelář, D. Matula, J. Holeček, J. Polym. Sci. Part A Polym. Chem. **34**, 2163 (1996)
10. V.A. Poluboyarov, V.F. Anufrienko, V.A. Zakharov, S.A. Sergeev, S.I. Makhtarulin, G.D. Bukatov, React. Kinet. Catal. Lett. **26**, 347 (1984)
11. A.A. Tregubov, V.A. Zakharov, T.B. Mikenas, Polym. Sci. A Polym. Chem. **47**, 6362 (2009)
12. E.I. Koshevoy, T.B. Mikenas, V.A. Zakharov, A.M. Volodin, R.M. Kenzhin, Catal. Commun. **48**, 38 (2014)
13. F. Allouche, D. Klose, C.P. Gordon, A. Ashuiev, M. Wörle, V. Kalendra, V. Mougel, C. Copéret, G. Jeschke, Angew. Chem. Int. Ed. **57**, 14533 (2018)
14. E. Morra, E. Giamello, S. Van Doorslaer, G. Antinucci, M. D'Amore, V. Busico, M. Chiesa, Angew. Chem. Int. Ed. **54**, 4857 (2015)
15. A. Piovano, K.S. Thushara, E. Morra, M. Chiesa, E. Groppo, Angew. Chem. Int. Ed. **55**, 11203 (2016)
16. E.I. Koshevoy, T.B. Mikenas, V.A. Zakharov, A.A. Shubin, A.A. Barabanov, J. Phys. Chem. C **120**, 1121 (2016)
17. S. Maurelli, E. Morra, S. Van Doorslaer, V. Busico, M. Chiesa, Phys. Chem. Chem. Phys. **16**, 19625–19633 (2014)
18. V.A. Zakharov, S.I. Makhtarulin, V.A. Poluboyarov, V.F. Anufrienko, Makromol. Chem. **185**, 178 (1984)
19. P. Höfer, A. Grupp, H. Nebenführ, M. Mehring, Chem. Phys. Lett. **132**, 279 (1986)
20. S. Stoll, A. Schweiger, J. Magn. Reson. **178**, 42 (2006)
21. A. Correa, R. Credendino, J.T.M. Pater, G. Morini, L. Cavallo, Macromolecules **45**, 3695 (2012)
22. A. Bazhenov, M. Linnolahti, T.A. Pakkanen, P. Denifl, T. Leinonen, J. Phys. Chem. C **118**, 4791 (2014)
23. M. D'Amore, K.S. Thushara, A. Piovano, M. Causà, S. Bordiga, E. Groppo, ACS Catal. **6**, 5786 (2016)
24. R. Credendino, V. Busico, M. Causà, V. Barone, P.H.M. Budzelaar, C. Zicovich-Wilson, Phys. Chem. Chem. Phys. **11**, 6525 (2009)
25. L. Brambilla, G. Zerbi, F. Piemontesi, S. Nascetti, G. Morini, J. Mol. Catal. A Chem. **263**, 103 (2007)
26. A. Abragam, B. Bleaney, *Electron Paramagnetic Resonance of Transition Ions* (Oxford University Press, Oxford, 1970)
27. P.L.W. Tregenna-Piggott, S.P. Best, M.C.M. O'Brien, K.S. Knight, J.B. Forsyth, J.R. Pilbrow, J. Am. Chem. Soc. **119**, 3324 (1997)
28. P.L.W. Tregenna-Piggott, C.J. Noble, J.R. Pilbrow, J. Chem. Phys. **113**, 3289 (2000)
29. R. Ameis, S. Kremer, D. Reinen, Inorg. Chem. **24**, 2751 (1985)
30. G. Corradi, I.M. Zaritskii, A. Hofstaetter, K. Polgár, L.G. Rakitina, Phys. Rev. B **58**, 8329 (1998)
31. E.S.M. Blaakmeer, F.J. Wensink, E.R.H. van Eck, G.A. de Wijs, A.P.M. Kentgens, J. Phys. Chem. C **123**, 14490–14500 (2019)